Journal of Materials Chemistry

Cite this: J. Mater. Chem., 2012, 22, 14076

www.rsc.org/materials

PAPER

Hierarchically aminated graphene honeycombs for electrochemical capacitive energy storage†‡

Cheng-Meng Chen,[abf] Qiang Zhang,[bc] Xiao-Chen Zhao,[bef] Bingsen Zhang,[bd] Qing-Qiang Kong,[a] Mang-Guo Yang,[a] Quan-Hong Yang,[a] Mao-Zhang Wang,[a] Yong-Gang Yang,[a] Robert Schlögl[b] and Dang Sheng Su*[bd]

Received 25th December 2011, Accepted 10th May 2012
DOI: 10.1039/c2jm31426f

Graphene with mediated surface properties and three-dimensional hierarchical architectures show unexpected performance in energy conversion and storage. To achieve advanced graphene electrode supercapacitors, manipulating the graphene building-blocks into hierarchical nanostructured carbon materials with large electrical double layer capacitance and pseudo-capacitance is a key issue. Here, it is shown that the hierarchically aminated graphitic honeycombs (AGHs) with large surface area for electrical double layer capacitance, tunable surface chemistry for pseudo-capacitance, mediated 3D macropores for ion buffering, and low-resistant pathways for ion diffusion are fabricated for electrochemical capacitive energy storage application through a facile high vacuum promoted thermal expansion and subsequent amination process. In the initial stage of amination (~200 °C), NH_3 reacts with carboxylic acid species to form mainly intermediate amides and amines through nucleophilic substitution. As the temperature increases, the intramolecular dehydration and decarbonylation will take place to generate thermally more stable heterocyclic aromatic moieties such as pyridine, pyrrole, and quaternary type N sites. The AGH exhibits a promising prospect in supercapacitor electrodes with high capacitance (*e.g.* maximum gravimetric capacitance 207 F g^{-1} and specific capacitance 0.84 F m^{-2} at a scan rate of 3 mV s^{-1}) and extraordinary stability (*e.g.* 97.8% of capacitance retention after 3000 cycles, and 47.8% of capacitance maintaining at a high scan rate of 500 mV s^{-1} comparing with that at 3 mV s^{-1}). This provides a novel structure platform for catalysis, separation, and drug delivery, which require fast mass transfer through mesopores, reactant reservoirs, and tunable surface chemistry.

1. Introduction

Three-dimensional (3D) hierarchical architectures of nanosheets, nanoplates, nanotubes, nanowires, and nanospheres, with unexpected properties in energy conversion and storage, nanocomposites, sustainable catalysis, optoelectronics, and drug delivery systems, have received great attention recently.[1,2] Among them, nanosheets, such as graphene and graphene oxide,[3–5] layered double hydroxides,[6] and natural clays,[7] were tested as possible building blocks for materials in energy conversion and storage. Among various energy storage routes, supercapacitors are gaining increasing attention for complementing batteries in hybrid electric vehicles, portable electronics, and industrial power management because of their large power density and longer cycle-life.[8,9] The key issue for the successful application of hierarchical architectures in energy storage lies in the ability to manipulate the arrangement of the building blocks into a well designed architectures. For this purpose, it is still a great challenge to select building blocks with high surface area for electrical double layer capacitance (EDLC), tunable surface chemistry for pseudo-capacitance (PC),

[a]Key Laboratory of Carbon Materials, Institute of Coal Chemistry, Chinese Academy of Sciences, 27 Taoyuan South Road, Taiyuan 030001, P. R. China
[b]Department of Inorganic Chemistry, Fritz Haber Institute of the Max Planck Society, Faradayweg 4-6, Berlin 14195, Germany. E-mail: dangsheng@fhi-berlin.mpg.de
[c]Beijing Key Laboratory of Green Chemical Reaction Engineering and Technology, Department of Chemical Engineering, Tsinghua University, Beijing 100084, P. R. China
[d]Catalysis and Materials Division, Shenyang National Laboratory for Materials Science, Institute of Metal Research, Chinese Academy of Sciences, 72 Wenhua Road, Shenyang 110016, P. R. China
[e]State Key Laboratory of Catalysis, Dalian Institute of Chemical Physics, Chinese Academy of Science, PO Box 110, Dalian, 116023, P. R. China
[f]Graduate University of the Chinese Academy of Sciences, 19A Yuquan Road, Beijing 100049, P. R. China

† All the electrochemical capacitive data in this paper are calculated based on a three-electrode system.

‡ Electronic supplementary information (ESI) available: XPS survey and C1s spectrum, MS curves and corresponding analysis of sweep gases from TG, various nitrogen and oxygen containing functional groups in carbon materials, collapse of honeycomb-like structure of AGHs after high temperature amination, chemically reduced graphene oxide by hydrazine hydrate, and comparison of performance of various carbon based supercapacitor electrodes. See DOI: 10.1039/c2jm31426f

accessible macropores for ion-buffering reservoirs, and low-resistant pathways for the charge carrier transport.

Graphene, the one-atom-thick two dimensional carbon crystal with excellent electronic conductivity and huge theoretical surface area (2630 $m^2 g^{-1}$), has been considered a novel component for supercapacitor electrodes.[10] Graphene sheets chemically derived from graphite oxide are intrinsically decorated by abundant active sites, such as functional groups (mainly –OH, –COOH, –C=O, –C–O–C–), lattice defects (atom vacancy, distortion, dangling bonds) on the lateral surface and at their edges.[11] Many active species such as conductive polymers (*e.g.* PANI),[12] metal oxide (*e.g.* RuO_2,[4] MnO_2 [5]), have been introduced to improve the PC as well as the whole performance of graphene based supercapacitor electrodes. However, such hybrids suffer from a rapid fading of capacity due to the large volumetric change or degradation during cycling. Therefore, exploring the basic building-blocks of graphene with large EDLC and PC due to fast and reversible surface redox processes between the electrolyte and various electro-active species on graphene electrode surface is still a great challenge.

Generally, heteroatom modification has been proven to be an efficient and effective way to tune the chemical and electrical environment of the carbon surface for catalysis and electrochemical process,[1] for instance, superior supercapacitor performance was available on heteroatom modified nanocarbon.[13,14] Recently, the individual graphene sheets can also be designed into various kinds of macroscopic hierarchical architectures (such as graphene oxide–graphene film,[15,16] hydrogel,[17] and foam[18]) with high electronic conductivity, large surface area, proper pore distribution, and superior mechanical and chemical properties.[15–18]

Based on this consideration, we explored the idea of constructing hierarchically aminated graphene honeycombs (AGHs) with large surface area, high charge carrier density, abundant PC-active sites with reversible Faradaic redox kinetics, and hierarchical 3D pores for advanced capacitive energy storage. The concept involves the exfoliation of bulk graphite oxide (GO) under high vacuum,[19] followed by amination of which at different temperatures. The microstructure and surface functionalities of AGHs were determined by high-angle annular dark-field (HAADF)-scanning transmission electron microscopy (STEM), electron energy loss spectroscopy (EELS), X-ray photoelectron spectroscopy (XPS) and thermogravimetry-mass spectroscopy (TG-MS), *etc.* In order to correlate the structural evolution with electrochemical performance of graphene, AGHs were further evaluated as the electrode materials for supercapacitor, and the maximum specific capacitance of 0.84 F m^{-2} and high retention rate of 97.8% after 3000 cycles were achieved.

2. Experimental

2.1. Preparation of hierarchically aminated graphitic honeycombs

The chemically derived graphene was obtained by low-temperature expansion of graphite oxide (GO) in high vacuum. GO was prepared by a modified Hummers method.[16] The as-prepared GO was put into a quartz tube that was sealed at one end and stopped at the other end, through which the reactor was connected to a vacuum pump. The tube was heated at a rate of 30 °C min^{-1} in high vacuum (<2 Pa). At about 195 °C, an abrupt expansion was observed. To remove the superabundant functional groups, the GO was kept at 250 °C for 30 min in high vacuum (below 5 Pa) to obtain G250. The G250 was placed uniformly in a quartz boat, and inserted into the center of a quartz tube (Φ 80 mm, L 1200 mm). The quartz tube was maintained at 200 °C with NH_3 flowing (200 mL min^{-1}) for 4.0 h to obtain AGH200. Meanwhile, AGH400 and AGH600 were also prepared by the similar procedures, with the only difference in amination temperature (400 and 600 °C, respectively).

The control experimental was conducted in a typical procedure as follows. GO (200 mg) was dispersed in 200 mL water followed by ultrasonication (200 W) for 30 min to yield a homogeneous brown solution. The above solution was mixed with hydrazine hydrate (50 mL, 100%) in a 500 mL round-bottom flask, and heated in an oil bath at 100 °C under a water-cooled condenser for 24.0 h over which the reduced GO gradually precipitated out as a black solid. This product was isolated by vacuum filtration and rinsed copiously with water (5 × 100 mL) and ethanol (5 × 100 mL). Finally, the sample was dried on the funnel under a continuous air flow through the solid product cake. The as-received control sample was denoted as CRG.

2.2. Sample characterization

The morphology of the samples was characterized by a Hitachi S4800 scanning electron microscope (SEM) operated at 2.0 kV and a Philips CM200 LaB_6 transmission electron microscope (TEM) operated at 200.0 kV. A FEI Cs-corrected Titan 80–300 microscope operated at 80.0 kV was employed to conduct structural investigations of AGH200 samples by using HAADF-STEM and EELS analysis. Energy dispersive X-ray spectroscopy (EDX) analysis was performed using a Titan 80–300 apparatus with the analytical software TIA, and the elemental mapping was conducted under STEM mode with the EDX detector as recorder. The AGH200 sample was ultrasonically dispersed in ethanol, and then a drop of the solution was deposited on a Lacey carbon film grid to be used for high resolution transmission electron microscopy (HRTEM) and HAADF-STEM characterization.

Laser Raman spectroscopy was performed on powder samples by using an ISA LabRam instrument equipped with an Olympus BX40 microscope. The excitation wavelength was 632.8 nm and a spectral resolution of 0.9 cm^{-1} was used. The N_2 sorption isotherm was obtained at 77 K using a Micromeritics 2375 BET apparatus, the specific surface area (S_{BET}) was determined by the BET method, the pore size distribution was deduced from the desorption isotherm by the BJH method, and the surface area of micropores (S_{micro}) was calculated by the t-plot approach (plot range from 3.5 nm to 5 nm). The TG-MS analysis was carried out on a TGA STA-449 Netsch apparatus equipped with a mass spectrometer (Pfeiffer Omnistar, Avi applied vacuum GmbH) in Ar atmosphere (10 °C min^{-1}, from room temperature to 1000 °C), the masses 17, 18, 28, and 44 were monitored for the detection of NH_3, H_2O, CO/N_2, and CO_2 with a time-resolution of 4 s. The XPS analysis was performed on the Thermo VG ESCALAB250 surface analysis system with parameters: AlKα = 1486.6 eV, power = 150 W (HV = 15 kV, I = 10 mA),

spot size = 500 μm, pass energy 50.0 eV, and energy step size 0.1 eV. The XP spectra were calibrated for both beam intensity and charging (reference B.E. at 284.4 eV of C1s peak). Prior to fitting, a Shirley background was subtracted. Peak areas were normalized with theoretical cross-sections to obtain the relative surface elemental compositions.

2.3. Electrochemical measurements

Electrochemical properties of G250, AGH200, AGH400, and AGH600 were measured in an aqueous system (electrolyte: 6.0 M KOH). A three-electrode system was employed in the measurements, whereas Ni foam coated with electrode materials served as the working electrode, a platinum foil electrode as the counter electrode and a saturated hydrogen electrode (SHE) as the reference electrode. In order to prepare a working electrode, a mixture of the active material, carbon black, and poly(tetrafluoroethylene) (PTFE) with a weight ratio of 80 : 5 : 15 was ground together to form a homogeneous slurry. The slurry was squeezed into a film and then punched into pellets (area ~0.8 cm^2). The punched pellets with a piece of nickel foam on each side were pressed under 2.5 MPa and dried overnight at 110 °C. Each electrode was quantified to contain ~3.5 mg active materials. The electrodes were saturated with the electrolyte by vacuum enhanced impregnation for 2.0 h prior to the test. Cyclic voltammetry (CV) curves (scan rates varying from 3 to 500 mV s^{-1}) and electrochemical impedance spectroscopy (EIS) profiles (frequency from 200 kHz to 10 mHz) were measured with a VSP BioLogic electrochemistry workstation. The gravimetric capacitances (C_F, F g^{-1}) was calculated from CV curves by equation:

$$C_F = \frac{1}{sm\Delta V}\int_{V_0}^{V_0+\Delta V} i\,dV$$

whereas s (mV s^{-1}) is the scan rate, m (g) is the mass of active materials in the electrode, ΔV (V) is the potential window (1 V in this work), V_0 (V) is the initial value of potential window (0 V in this work), and i (A) is the real time current during scanning. The Nyquist plots were fitted by EC-Lab software with the equivalent circuit as $R_c + C_c/(R_i + W) + C_d$, the Randomize plus Levenberg–Marquardt method was employed for the fitting. The Ragone plot was calculated from CV results, the energy density (E, Wh kg^{-1}) was calculated by equation: $E = 1/2(C_F/4)\Delta V^2$, while power density (P, W kg^{-1}) was calculated by: $P = E/t$, where t (s) is the current drain time of discharging.[20,21]

3. Results and discussion

3.1. The microstructure of AGHs

With the promotion of an external high vacuum environment, the initial graphene honeycomb G250 is available at a relative lower temperature (250 °C) compared with the normal thermal expansion approach.[22] Abundant oxygen functionalities are preserved during exfoliation, as shown in Table 1, the G250 maintains a high oxygen content of 10.74 at%. The G250 is further treated in ammonia under 200, 400, and 600 °C for 4 h, and the as-obtained hierarchically aminated graphene honeycombs are denoted as AGH200, AGH400, and AGH600, respectively. The representative SEM images of AGH200 are shown in Fig. 1a and b. The N modified graphene sheets are loosely stacked or folded with each other to construct continuous and interconnected 3D macroscopic honeycombs, with a specific BET area of ~247 m^2 g^{-1}. Most of the graphene sheets are crumpled with many ripples and wrinkles on their surfaces. Large porous network with size ranging from 30 to 200 nm is clearly visible among the lateral edges of multilayer graphene. The unique macroscopic honeycomb-like structure is believed to be generated during thermal exfoliation process, where a negative pressure was surrounding the bulk graphite oxide to cause a moderate interlayer expansion. Moreover, these pores can be well preserved during low temperature (200 °C) amination for hierarchical AGHs.

TEM, HAADF-STEM, and EDX elemental mapping techniques were employed to characterize the microtexture and chemical construction of the basic building blocks of AGH200. The TEM and STEM images (Fig. 1c and d) indicate that the graphene sheets are micrometer-sized curved flakes, with a high transparency chiffon-like texture. The HAADF image (Fig. 1e) and C, N, O elemental maps of a selected zone (Fig. 1f–h) illustrate a homogeneous distribution of N and O functionalities on graphene. Different from the conventional electrode materials such as activated carbons with wormlike pores, the exterior porous structure of 3D assembly and uniform functionalization of 2D building blocks will make the active surface of graphene extraordinary accessible to the ions of electrolyte in the solution-based electrochemical processes.

3.2. The surface chemistry of AGHs

The evolution of surface chemistry from G250 to AGHs is investigated by XPS. The survey spectra and C1s fine scan spectra are shown in Fig. S1‡, while the relative abundance of C, N and O elements on the surface of sample is calculated accordingly, as summarized in Table 1. With the increase of amination temperature, oxygen atoms are gradually removed (10.74 at% for G250 to 5.23 at% for AGH600) with a simultaneous introduction of nitrogen (2.79 at% for AGH200 to 3.91 at % for AGH600). It is noteworthy that AGH200 has the maximum heterogeneity (N + O ~ 13.09 at%) among all the samples. Various N (N1–N5) and O (O1–O5) components in AGHs are further determined by fitting N1s (Fig. 2a) and O1s (Fig. 2b) spectra. The assignment and quantification of nitrogen and oxygen components are summarized in Tables 2 and 3, respectively. N1 (398.1 eV), N2 (399.3 eV), N3 (400.6 eV), N4 (402.1 eV), and N5 (403.8 eV) species are assigned to pyridinic, amine/amide, pyrrole/pyridine, quaternary nitrogen (N atoms incorporated in the graphitic layer in substitution of C atoms), and N-oxide/nitro, respectively. While O1 (530.4 eV), O2 (531.2 eV), O3 (531.9 eV), O4 (532.8 eV), and O5 (533.4 eV) components are assigned to quinones, COOH/C(O)O, –C═O, –C–O and –OH related groups, respectively.[23]

As shown in Table 3, the pristine G250 contains abundant oxygen functional groups (–COOH, –OH, –C–O–C–, and –C═O), which has already been confirmed by previous reports.[24,25] After amination at 200 °C, the amine/amide-type N atoms chemically bonded to graphene ("chemical nitrogen") are initially introduced as the primary N species in AGH200. With the increase of amination temperature, more pyridinic, pyrrolic

Table 1 Parameters on pore structure and elemental composition

Sample	S_{BET}[a] ($m^2\ g^{-1}$)	S_{micro}[a] ($m^2\ g^{-1}$)	V_P[a] ($cm^3\ g^{-1}$)	C[b] (at%)	O[b] (at%)	N[b] (at%)	O + N[b] (at%)	Residual carbon[c] (wt%)
G250	293.2	3.663	3.58	89.26	10.74	0.00	10.74	62.6
AGH200	247.0	NA	3.40	86.91	10.30	2.79	13.09	71.1
AGH400	703.5	NA	3.32	87.87	8.39	3.74	12.13	84.3
AGH600	503.0	NA	3.17	90.86	5.23	3.91	9.14	91.1
CRG	666.0	69.93	0.55	88.43	11.57	0.00	10.74	—

[a] Obtained from N_2 adsorption–desorption isotherm. [b] Quantified by XPS. [c] Obtained from TGA (from room temperature to 1000 °C with a rate of 10 °C min^{-1} in Ar).

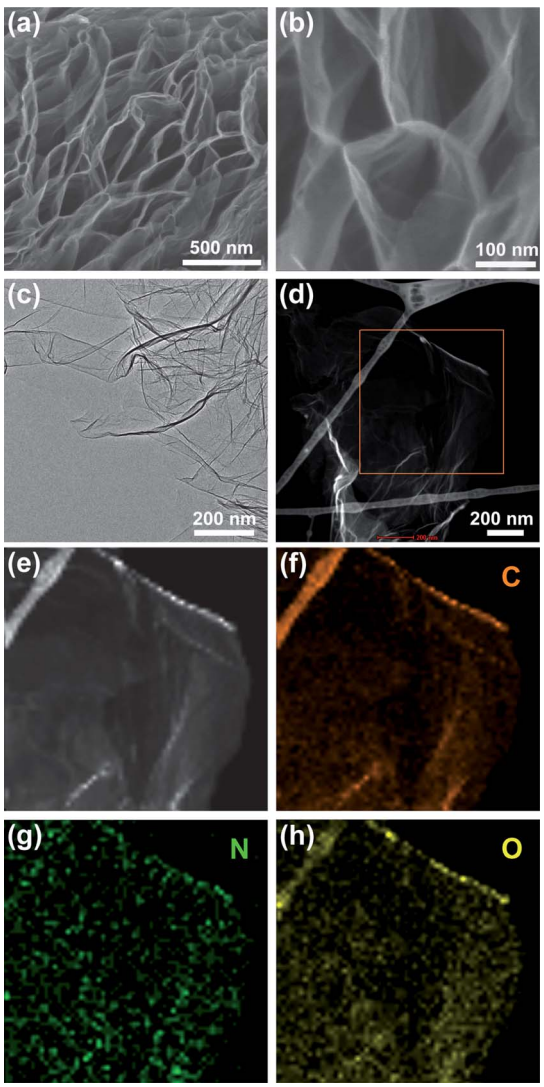

Fig. 1 Microstructure of AGHs: (a–b) SEM, (c) TEM, (d–e) HAADF-STEM, and (f–h) C, N, O elemental maps of AGH200.

and quaternary type N atoms ("lattice nitrogen") which substitute carbon in the matrix are increasing gradually with a simultaneous decrease of thermally unstable "chemical nitrogen".[26] At the same time, the acidic –COOH groups and –C–O related species are decreasing remarkably from G250 to AGH600 (from 1.63 to 0.81 at% for –COOH, and from 3.31 to 1.39 at% for –C–O). Meanwhile, –C═O and –OH species in AGH200 are

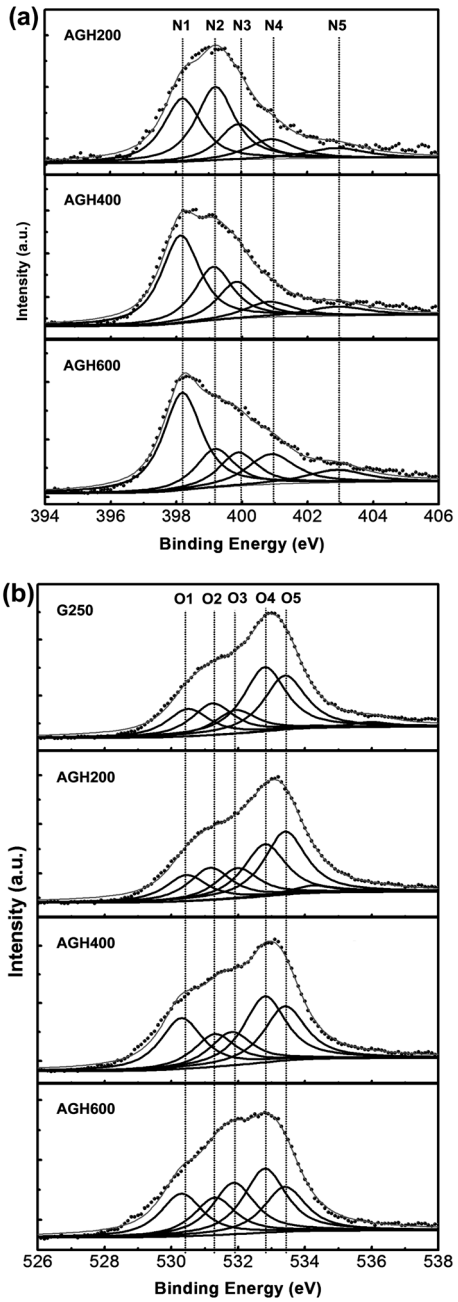

Fig. 2 XPS Analysis of G250 and AGHs: fitting results of (a) N1s and (b) O1s fine scan spectrum.

Table 2 Summary of nitrogen containing functional groups in AGHs

B.E (eV)	N1 (398.1)	N2 (399.3)	N3 (400.6)	N4 (402.1)	N5 (403.8)
Species	Pyridinic	Amine/amide	Pyrrole/pyridone	Quaternary	N-oxide/nitro
G250	0	0	0	0	0
AGH200	0.84	0.96	0.46	0.33	0.19
AGH400	1.57	0.94	0.65	0.34	0.24
AGH600	1.71	0.66	0.58	0.65	0.32

increased to a maximum ratio of 1.47 and 3.05 at%, respectively. However, the two species will be gradually diminished in AGH400 and AGH600.

The decreasing of O at% and simultaneous increasing of N at% from G250 to AGH600 indicate that a portion of oxygen sites and lattice defects on graphene are incorporated with or substituted by N-containing functional groups during amination, while another amounts of O species are temperately removed in the form of small molecules (*e.g.* H_2O, CO and CO_2).[25,27] Besides, the increasing of C1s intensity at 284.4 eV from G250 to AGH600, as shown in Fig. S1b‡, indicate the restoration of sp^2 conjugated basal plane of the graphene lattice due to the removal and/or stabilization of sp^3 saturated oxygen functionalities.

In accordance with the XPS results, N and O K-edges in EELS spectroscopy illustrates a similar tendency (Fig. 3a). The carbon K-edge EELS spectra clearly show two energy loss features. The first narrow peak at around 284 eV corresponds to an electronic transition from carbon 1s to anti-bonding π^* states, which is the characteristic of sp^2-bonded carbon, while the broader structure at 290–310 eV indicates transitions to antibonding σ^* states. The distances between π^* and σ^* peaks for C (7.56 eV) and N (7.59 eV) species are almost the same, which indicate a homogeneous bulk doping of N atoms in AGHs.

Raman spectroscopy is introduced to investigate the graphitic and disordered regions of the materials (Fig. 3b). The peak at around 1339 cm^{-1} is attributed to the disorder-induced band of graphitic carbon (D band), while the peak at around 1591 cm^{-1} is assigned to in-plane vibrations of graphite (sp^2-bonded carbon; G band). With the increase of amination stage, the integrated intensity ratio of the D and G bands (A_D/A_G) increases progressively from 2.53 of G250 to 2.97 of AGH600, due to the amorphization of graphitic domains in graphene during amination. On one hand, the introduction of nitrogen, especially the "lattice N" which is directly bonded to in-plane sp^2 carbons will cause the lattice distortion of graphitic region so as to transform into sp^3 domain. On the other hand, the simultaneous thermal evolution of oxygen such as ether-type groups will create various atomic vacancies and may even crack the graphene sheets. Thereafter, numerous sp^2 graphitic domains with smaller sizes, which are separated by newly introduced amorphous regions, are generated during the thermal amination process.

The N_2 sorption of AGH200 (Fig. 3c) exhibit a type III adsorption isotherm with H3 hysteresis loop in IUPAC classification, indicating a unique adsorption behavior in the slit-shaped macropores raised from aggregates of plate-like particles. As shown in the BJH adsorption pore size distribution (inset of Fig. 3c), very little amount of pore volume of AGH200 is contributed by micropores (Φ < 2 nm). In addition, the associated pore volume increases gradually with the increase of pore diameter, confirming the exterior macroporous structure of AGHs by SEM observation.

The surface chemistry of graphene (especially the relative abundance of various functional groups) is largely dependent on the temperature employed for amination, which is attributed from the huge difference in thermal stability of various N and O groups.[27] Hereby, the TG-MS method is employed to characterize the thermochemistry of G250 and AGHs in inert atmosphere (TG in Fig. 3d and MS in Fig. S2‡), the residual carbon of the materials after annealing to 1000 °C are summarized in Table 1. From G250 to AGH600, the residual carbon are increasing significantly. It is interesting that the residual carbon of AGH200 (71.1%) is higher than that of G250 (62.6%), though AGH200 (13.09 at%) exhibits a higher heteroatomic ratio than G250 (10.74 at%). The sweep gases from TG are further analyzed by mass spectrometry, various fragments (*e.g.* CO_2, CO, NH_3, H_2O and radical C) are detected and assigned (Table S1‡). After low temperature amination, the amount of evolved carbon-containing gases (such as radical C, CO and CO_2) decreases significantly for AGH200, with a corresponding blue shift of the desorption temperatures for the functional groups. This indicates that the unstable defects and oxygen functionalities (–C=O, –COOH) in the disordered sp^3 regions of graphene are efficiently stabilized with a simultaneous N doping during low temperature amination (<200 °C). When the amination is carried out at relatively higher temperatures (*e.g.* 400 and 600 °C), most of the thermally unstable species (–COOH, $–NH_2$) are intensively removed or transformed into stable ones.

Table 3 Summary of oxygen containing functional groups in AGHs

B.E. (eV)	O1 (530.4)	O2 (531.2)	O3 (531.9)	O4 (532.8)	O5 (533.4)
Species	Quinones	COOH	C=O	C–O	OH
G250	1.42	1.63	1.22	3.31	2.78
AGH200	1.27	1.57	1.47	2.53	3.05
AGH400	1.80	1.15	1.19	2.34	1.92
AGH600	0.93	0.81	1.12	1.39	0.97

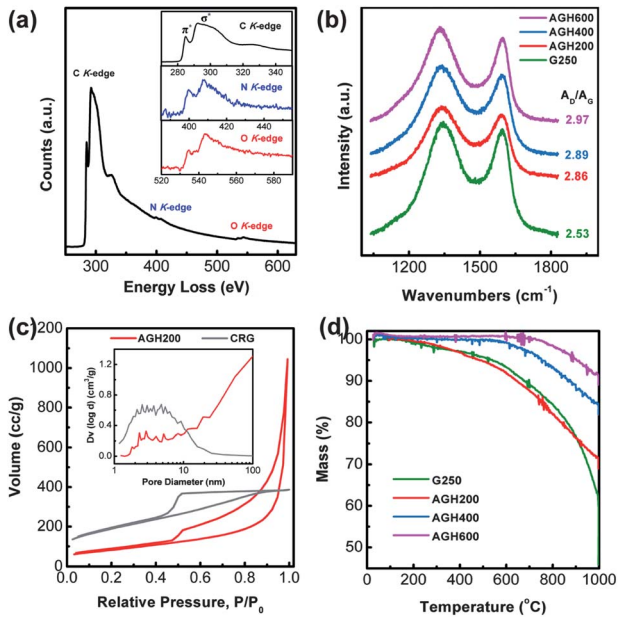

Fig. 3 Chemical analysis: (a) EELS spectra of AGH200, (b) Raman evolution from G250 to AGHs, (c) N_2 sorption isotherm and inset pore size distribution of AGH200 and CRG, and (d) TGA curves of G250 and AGHs.

The forms and chemical evolution of N and O functional groups in different carbon allotropes (*e.g.* carbon black,[28] activated carbon,[29] carbon nanotubes,[23] and graphene[25,30]) have been intensively studied in the past several decades. The possible N and O containing functional groups in aminated carbon materials are depicted in Fig. S3. It has been reported that the sequence of thermal stability for the oxygen groups on carbon surface is: carbonyl > hydroxyl > epoxy > carboxyl.[25,27] As shown in Fig. 4, in the initial amination stage (*e.g.* below 200 °C), NH_3 reacts with carboxylic acid species to form mainly intermediate amide or amine like species ("chemical N") through nucleophilic substitution. As the temperature increases (*e.g.* 200–400 °C), the intramolecular dehydration or decarbonylation will take place to generate thermally stable heterocyclic aromatic moieties such as pyridine, pyrrole and quaternary type N sites ("lattice N").

3.3. The electrochemical capacitance of AGH

In order to evaluate the electrochemical energy-storage performance of as prepared materials, the G250 and AGHs are

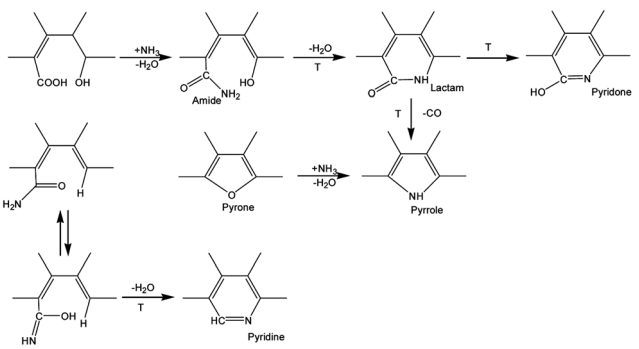

Fig. 4 The proposed pathways for N insertion into graphene.

characterized by CV with 6.0 M KOH aqueous solution as the electrolyte. The CV curves at a slow scan rate of 3 mV s^{-1}, as shown in Fig. 5a, illustrate the capacitive behavior of G250 and AGHs based electrodes. Comparing with G250, AGH200 exhibits a significant enhancement of PC contribution in the potential range from −0.1 V to 0.4 V, while AGH400 and AGH600 represents an increased ratio of EDLC character with a more rectangular shape in CV patterns. The capacitance values of G250, AGH200, AGH400, and AGH600 are given in Fig. 5b and c. Among all samples, AGH200 exhibits the most prominent performance in energy storage. The gravimetric capacitance C_F and specific capacitance C_s of AGH200 reach values as high as 207 F g^{-1} and 0.84 F m^{-2} (scan rate 3 mV s^{-1}), which are improved by 19 and 42%, respectively, comparing with G250.

The improvement of capacitive performance from G250 to AGH200 is mainly attributed to the introduction of extra PC-active N species on the basis of well protection of 3D honeycomb-like structure at a very mild temperature of 200 °C. Besides, the abundant original O containing functional groups in G250, which are believed to contribute abundant PC-active sites to CDGs,[31] can also be well preserved in the mild amination. Thus, the co-presented O and N heteroatoms, which substitute for carbon or occurring as functional groups, are highly concerned in modifying the electron donor–acceptor properties and acid–basic character. This can further influence the electrochemical performance by affecting charging of the EDLC and to give extra PC.[8]

The mechanism of O and N atoms in enhancing the capacitance by reversible Faradic redox reactions in the aqueous electrolyte has been widely studied.[8,21] As the individual functional graphene sheet is composed of sp^2 conjugated aromatic domains

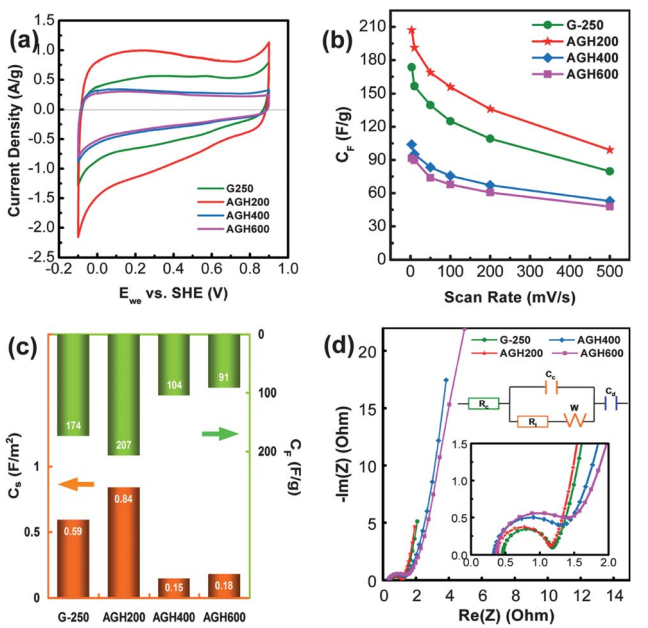

Fig. 5 Electrochemical performance of G250 and AGHs: (a) CV curves at 3 mV s^{-1} in an alkaline electrolyte (6.0 M KOH); (b) gravimetric capacitance as a function of potential scan rates (from 3 to 500 mV s^{-1}); (c) gravimetric and specific capacitance at 3 mV s^{-1}; and (d) nyquist plots of AC impedance spectra.

decorated by abundant N and O functionalities, the abundant delocalized electrons from the conjugated π bonds of graphitic domains and the extra lone pair electrons donated by the "lattice N" provide a low resistant pathway for charge transfer in the electrode. While the inductive effects of the σ-bonded structure from O and N heteroatoms will cause a redistribution of the electrons as well as the polarization of some bonds. Thus, as depicted in Fig. 6, in the aqueous electrolyte, the electric potential induced redox reactions of these polarized sites will take place through the reversible gaining/losing of electrons and simultaneous adsorption/desorption of protons, respectively. In addition, the acidic functional sites such as –COOH (II), –OH (III) and pyrrolic N (VII), which are well maintained or additionally introduced after amination at 200 °C, may play the key role in reversible Faradic redox reactions for enhanced PC in alkaline aqueous electrolyte (such as 6.0 M KOH employed in this work). As a result, the specific capacitance of AGH200 is higher than that of most nanocarbon materials (see Table S2‡), which is attributed to the efficient EDLC and PC contributions from each nanosheet within the hierarchical honeycomb architecture.

However, though amination seems to be an efficient approach in enhancing the electrochemical performance of graphene-based

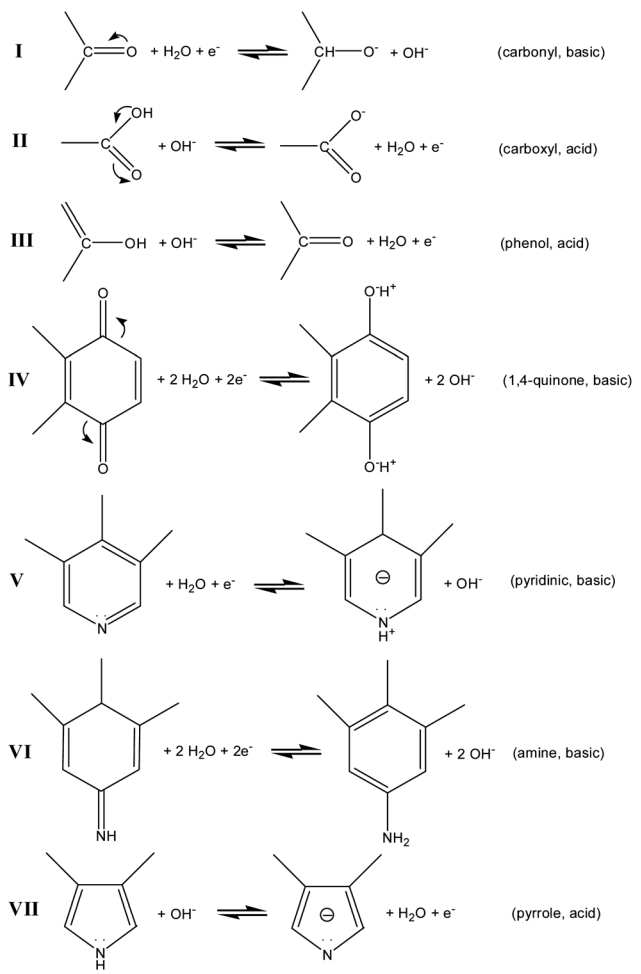

Fig. 6 The proposed reversible pseudo-capacitive reactions of various functional sites.

electrode, the maximum temperature employed for it should be properly adjusted. For example, the gravimetric capacitance of AGH400 (scan rate: 3 mV s^{-1}, C_F = 104 F g^{-1}) slumps to only ~50% of AGH200, which result in a very poor specific capacitance (C_s) of only 0.15 F m^{-2}. On one hand, for AGH400 and AGH600, though more N atoms are introduced, the total amount of heteroatom functionalities decreases significantly for an intensive removal of oxygen at high temperature, especially for the loss of some PC-active species (*e.g.* –C=O, –COOH and –OH). On the other hand, a higher treatment temperature of 400 or 600 °C will cause the collapse of hierarchical honeycomb-like structure (Fig. S4‡). Though AGH400 and AGH600 have higher BET areas of 703 and 500 m^2 g^{-1} respectively, the total pore volumes of both samples decreased and no micropore can be deduced from the *t*-plot analysis (Table 1). The above SEM and BET results imply that more lattice defects are introduced to the basal plane of graphene and may even cause the crack of which into smaller pieces during the harsh NH_3 activation at higher temperature.

It is worth mentioning that the gravimetric capacitance of AGH200 maintain a very high retention of 47.8% with a high scan rate of 500 mV s^{-1}. This value is much higher than the conventional carbon electrode materials, such as activated carbon or mesoporous carbon (usually 20–30%),[32] which is attributed to the 3D porous structure and tunable surface properties of AGHs. Firstly, the high content of oxygen and nitrogen provides large amount of active sites for PC, due to their reversible redox reactions with ions in the electrolyte.[13,33] Secondly, the introduction of nitrogen as electron donor significantly increases the charge carrier density in the basal plane,[34] and the removal of some excessive oxygen groups effectively restored the sp^2 conjugated basal plane of graphene sheet. Thus, the conductivity of aminated graphene is correspondingly improved to render a facile electron transfer during the electrochemical charge–discharge process. Finally, the AGH features a 3D structure with macro-pores serving as ion-buffering reservoirs, mesoporous walls guaranteeing a smaller ion-transport resistance and large graphene surface accommodating charges.[35] Therefore, the AGH materials show a promising prospect towards energy storage applications of fast charge–discharge capabilities.

To further confirm the double layer formation, AC impedance spectroscopy is employed to distinguish the resistance and capacitance of the electrodes (Fig. 5d). An equivalent circuit model (inset of Fig. 5d) is introduced to simulate the capacitive and resistive elements of the cells under analysis.[36] These elements include the internal resistance (R_i) of the AGH based electrode, the capacitance and resistance due to contact interface (C_c and R_c), a Warburg diffusion element attributable to the ion migration through the AGH (Z_w), and the capacitance inside the pores (C_d). The fitting results are shown in Table 4. In accordance with the microstructural and chemical evolution of graphene, the internal resistance (R_i) of AGH200 (0.38 Ω) is lower than the unaminated G250 (0.46 Ω). The reason is attributed to the effect of deoxygenation and nitrogen modification during amination, which not only restore the sp^2 conjugated carbon lattice, but also increase the charge carrier density. Moreover, comparing with G250 (Z_w = 0.76 Ω $S^{1/2}$), AGH200 exhibits a lower Warburg diffusion resistance (Z_w = 0.66 Ω $S^{1/2}$), which is

Table 4 Components of the equivalent circuit fitted for the impedance spectra

Sample	R_i (Ω)	R_c (Ω)	C_c (F g^{-1})	W (Ω S$^{-1/2}$)	C_d (F g^{-1})
G250	0.46	0.68	0.11	0.76	153.6
AGH200	0.38	0.73	0.24	0.66	192.2
AGH400	0.34	0.91	0.39	2.05	38.1
AGH600	0.37	0.99	0.54	2.49	36.2

an indicator for improvement of ion transfer between inner channel of electrode and electrolyte. As a result, the inner-porous specific capacitance (C_d) of AGH200 could reach as high as 192.2 F g^{-1}, which is improved by ~25.1% comparing with the unaminated G250 (C_d = 153.6 F g^{-1}) (Table 4).

In order to verify the contribution of the opened porous honeycomb structure in the electrode, a further control experiment with chemically reduced GO (denoted as CRG) obtained *via* a typical liquid phase reduction of GO by hydrazine hydrate is also performed. The CRG presents a disorderly packed morphology of agglomeration without hierarchical honeycomb structure (Fig. S5a‡). It owns a high BET surface area of 666 m^2 g^{-1} and a considerable initial C_F of 169 F g^{-1} at 3 mV s^{-1}. However, the C_F of CRG falls sharply to only 10.8% at 500 mV s^{-1} (Fig. S5b‡). The N_2 sorption isotherm of CRG (Fig. 3c) reveals the formation of ink-bottle pores, due to the over-compact agglomeration of graphene sheets during chemical reduction and drying process. The huge surface area of CRG is mainly contributed by the micro- and mesopores with diameter of less than 11 nm, which is definitely different from exterior macroporous structure of AGH200 (inset of Fig. 3c and Table 1). The "necking" effect of these ink-bottle pores and internal worm-like channels will hamper the mass transfer and thus slow down the ion diffusion in CRG. The above result, from another perspective, further confirms the huge contribution of 3D hierarchical honeycomb structure in enhancing the fast charge–discharge capabilities of supercapacitor electrodes.

A Ragone plot of AGHs is exhibited in Fig. 7a. The energy and power densities were calculated by means of CV curves of a supercapacitor using a cell-voltage window of 1.0 V.[20] Over a wide range of current drain time from 2 to 360 s, AGH200 holds an energy density of no less than 3.4 Wh kg^{-1}, with a corresponding power density as high as 6193 W kg^{-1}, which is far beyond the normally used lithium ion batteries with a power density of less than 500 W kg^{-1}. At a long current drain time of 360 s, the energy density of AGH200 could approach 7.2 Wh kg^{-1}, which is approaching that of commercial lead-acid batteries.

The cycle life of AGH electrode was evaluated by repeating CV charge–discharge process at a scan rate of 50 mV s^{-1}. As shown in Fig. 7b, after 3000 times of cycling, the gravimetric capacitance still maintain a high retention of 97.8%, with only a tiny pattern change in CV curves. Comparing with the other energy storage devices which often suffer from a short cycle life due to irreversible physical and/or chemical changes, AGH based supercapacitor exhibits a prominent performance in durability and stability.

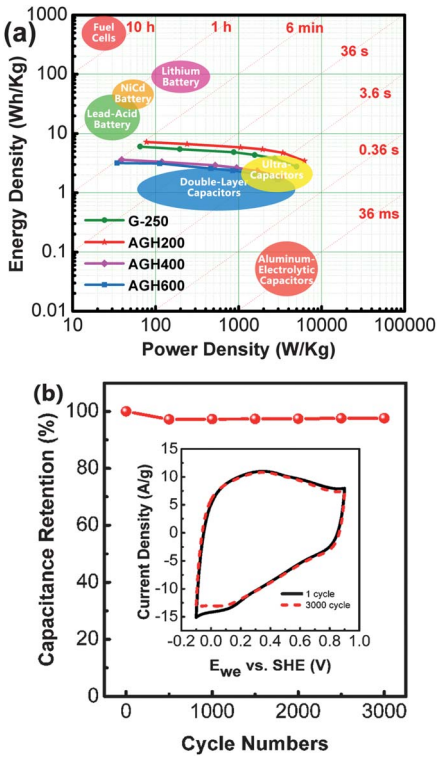

Fig. 7 Energy storage performance of AGHs: (a) Ragone plot showing the performance of graphene honeycomb based supercapacitor electrodes among various commercial energy-storage devices (source data from US Defense Logistics Agency) and (b) cycling performance of AGH200. Inset shows the 1 and 3000 cycle CV of AGH200 at a scan rate of 50 mV s^{-1} in 6.0 M KOH.

4. Conclusions

Hierarchically aminated graphene honeycombs are obtained through vacuum assisted thermal expansion of graphite oxide followed by amination. When the amination temperature is low (such as 200 °C), NH_3 reacts with carboxylic acid species to form mainly intermediate amide or amine like species ("chemical N") through nucleophilic substitution. When the amination temperature increases, the intramolecular dehydration or decarbonylation will take place to generate thermally stable heterocyclic aromatic moieties such as pyridine, pyrrole and quaternary type N sites ("lattice N"). This functional 3D assembly of graphene shows a promising prospect in electrochemical capacitive energy storage with high capacitance (*e.g.* gravimetric capacitance 207 F g^{-1} and specific capacitance 0.84 F m^{-2} at 3 mV s^{-1}) and long cycle-life (*e.g.* 97.8% of retention rate after 3000 cycles, and maintains 47.8% of capacitance at 500 mV s^{-1} comparing with 3 mV s^{-1}). The outstanding performance of AGH in energy storage is attributed to: (i) PC enhancement by chemical modification of the 2D basic building block-graphene (*e.g.* surface functionalization, polarity, charge carrier and acid–base properties); (ii) ion diffusion improvement through structural optimization of 3D honeycomb nano-structure (*e.g.* pore size distribution, pore volume and surface accessibility). In prospect, this indicates a promising way for hierarchical graphene honeycombs with tunable surface chemistry and mediated porous structure. The

integration of graphene into hierarchical structures provides a maximum utilization of the excellent properties of graphene and could lead to promising 3D macrostructures. Such porous hierarchical architectures will benefit applications in heterogeneous catalysis, separation, and drug delivery, which requires fast mass transfer through mesopores, reactant reservoirs, and tunable surface chemistry.

Acknowledgements

The authors greatly appreciate financial support by the EnerChem project of the Max Planck Society. The authors gratefully acknowledge Sylvia Reiche for fruitful discussions, and Thomas Patric Cotter, Gisela Lorenz, Edith Kitzelmann, Frank Girgsdies, Raoul Blume, Adriana Bernal Osorio, and Jutta Kröhnert for experimental assistance. C.M.C. also appreciates the sponsorship from the "Joint PhD Promotion Programme 2010" between the Max Planck Society and the Chinese Academy of Sciences.

Notes and references

1 D. S. Su and R. Schlogl, *ChemSusChem*, 2010, **3**, 136.
2 C. Liu, F. Li, L. P. Ma and H. M. Cheng, *Adv. Mater.*, 2010, **22**, E28.
3 J. J. Xu, K. Wang, S. Z. Zu, B. H. Han and Z. X. Wei, *ACS Nano*, 2010, **4**, 5019; Z. J. Fan, J. Yan, L. J. Zhi, Q. Zhang, T. Wei, J. Feng, M. L. Zhang, W. Z. Qian and F. Wei, *Adv. Mater.*, 2010, **22**, 3723; S. B. Yang, G. L. Cui, S. P. Pang, Q. Cao, U. Kolb, X. L. Feng, J. Maier and K. Mullen, *ChemSusChem*, 2010, **3**, 236; D. S. Yu and L. M. Dai, *J. Phys. Chem. Lett.*, 2010, **1**, 467; S. S. Li, Y. H. Luo, W. Lv, W. J. Yu, S. D. Wu, P. X. Hou, Q. H. Yang, Q. B. Meng, C. Liu and H. M. Cheng, *Adv. Energy Mater.*, 2011, **1**, 486.
4 Z. S. Wu, D. W. Wang, W. Ren, J. Zhao, G. Zhou, F. Li and H. M. Cheng, *Adv. Funct. Mater.*, 2010, **20**, 3595.
5 Z. J. Fan, J. Yan, T. Wei, L. J. Zhi, G. Q. Ning, T. Y. Li and F. Wei, *Adv. Funct. Mater.*, 2011, **21**, 2366.
6 M. Q. Zhao, Q. Zhang, X. L. Jia, J. Q. Huang, Y. H. Zhang and F. Wei, *Adv. Funct. Mater.*, 2010, **20**, 677; M.-Q. Zhao, Q. Zhang, J.-Q. Huang and F. Wei, *Adv. Funct. Mater.*, 2012, **22**, 675.
7 Q. Zhang, M. Q. Zhao, Y. Liu, A. Y. Cao, W. Z. Qian, Y. F. Lu and F. Wei, *Adv. Mater.*, 2009, **21**, 2876.
8 E. Frackowiak, *Phys. Chem. Chem. Phys.*, 2007, **9**, 1774.
9 L. L. Zhang and X. S. Zhao, *Chem. Soc. Rev.*, 2009, **38**, 2520; P. Simon and Y. Gogotsi, *Nat. Mater.*, 2008, **7**, 845; H. Zhang, G. P. Cao and Y. S. Yang, *Energy Environ. Sci.*, 2009, **2**, 932; G. Lota, K. Fic and E. Frackowiak, *Energy Environ. Sci.*, 2011, **4**, 1592.
10 K. S. Novoselov, A. K. Geim, S. V. Morozov, D. Jiang, Y. Zhang, S. V. Dubonos, I. V. Grigorieva and A. A. Firsov, *Science*, 2004, **306**, 666; M. D. Stoller, S. J. Park, Y. W. Zhu, J. H. An and R. S. Ruoff, *Nano Lett.*, 2008, **8**, 3498; H. Bai, C. Li and G. Q. Shi, *Adv. Mater.*, 2011, **23**, 1089; S. J. Guo and S. J. Dong, *Chem. Soc. Rev.*, 2011, **40**, 2644; Y. W. Zhu, S. Murali, M. D. Stoller, K. J. Ganesh, W. W. Cai, P. J. Ferreira, A. Pirkle, R. M. Wallace, K. A. Cychosz, M. Thommes, D. Su, E. A. Stach and R. S. Ruoff, *Science*, 2011, **332**, 1537; Y. Q. Sun, Q. O. Wu and G. Q. Shi, *Energy Environ. Sci.*, 2011, **4**, 1113.
11 K. P. Loh, Q. L. Bao, P. K. Ang and J. X. Yang, *J. Mater. Chem.*, 2010, **20**, 2277; Y. W. Zhu, S. Murali, W. W. Cai, X. S. Li, J. W. Suk, J. R. Potts and R. S. Ruoff, *Adv. Mater.*, 2010, **22**, 3906; H. T. Liu, Y. Q. Liu and D. B. Zhu, *J. Mater. Chem.*, 2011, **21**, 3335.
12 D. W. Wang, F. Li, J. P. Zhao, W. C. Ren, Z. G. Chen, J. Tan, Z. S. Wu, I. Gentle, G. Q. Lu and H. M. Cheng, *ACS Nano*, 2009, **3**, 1745; S. B. Yang, X. L. Feng, L. Wang, K. Tang, J. Maier and K. Mullen, *Angew. Chem., Int. Ed.*, 2010, **49**, 4795.
13 D. Hulicova-Jurcakova, M. Seredych, G. Q. Lu and T. J. Bandosz, *Adv. Funct. Mater.*, 2009, **19**, 438.
14 H. M. Jeong, J. W. Lee, W. H. Shin, Y. J. Choi, H. J. Shin, J. K. Kang and J. W. Choi, *Nano Lett.*, 2011, **11**, 2472; X. C. Zhao, Q. Zhang, B. S. Zhang, C. M. Chen, A. Q. Wang, T. Zhang and D. S. Su, *J. Mater. Chem.*, 2012, **22**, 4963.
15 D. A. Dikin, S. Stankovich, E. J. Zimney, R. D. Piner, G. H. B. Dommett, G. Evmenenko, S. T. Nguyen and R. S. Ruoff, *Nature*, 2007, **448**, 457; X. L. Li, G. Y. Zhang, X. D. Bai, X. M. Sun, X. R. Wang, E. Wang and H. J. Dai, *Nat. Nanotechnol.*, 2008, **3**, 538; F. Kim, L. J. Cote and J. X. Huang, *Adv. Mater.*, 2010, **22**, 1954; S. Park, N. Mohanty, J. W. Suk, A. Nagaraja, J. H. An, R. D. Piner, W. W. Cai, D. R. Dreyer, V. Berry and R. S. Ruoff, *Adv. Mater.*, 2010, **22**, 1736; X. W. Yang, J. W. Zhu, L. Qiu and D. Li, *Adv. Mater.*, 2011, **23**, 2833.
16 C. M. Chen, Q. H. Yang, Y. G. Yang, W. Lv, Y. F. Wen, P. X. Hou, M. Z. Wang and H. M. Cheng, *Adv. Mater.*, 2009, **21**, 3007.
17 Y. X. Xu, K. X. Sheng, C. Li and G. Q. Shi, *ACS Nano*, 2010, **4**, 4324.
18 Z. H. Tang, S. L. Shen, J. Zhuang and X. Wang, *Angew. Chem., Int. Ed.*, 2010, **49**, 4603; S. H. Lee, H. W. Kim, J. O. Hwang, W. J. Lee, J. Kwon, C. W. Bielawski, R. S. Ruoff and S. O. Kim, *Angew. Chem., Int. Ed.*, 2010, **49**, 10084; Z. P. Chen, W. C. Ren, L. B. Gao, B. L. Liu, S. F. Pei and H. M. Cheng, *Nat. Mater.*, 2011, **10**, 424.
19 W. Lv, D. M. Tang, Y. B. He, C. H. You, Z. Q. Shi, X. C. Chen, C. M. Chen, P. X. Hou, C. Liu and Q. H. Yang, *ACS Nano*, 2009, **3**, 3730.
20 R. Kotz and M. Carlen, *Electrochim. Acta*, 2000, **45**, 2483.
21 E. Frackowiak and F. Beguin, *Carbon*, 2001, **39**, 937.
22 H. C. Schniepp, J. L. Li, M. J. McAllister, H. Sai, M. Herrera-Alonso, D. H. Adamson, R. K. Prud'homme, R. Car, D. A. Saville and I. A. Aksay, *J. Phys. Chem. B*, 2006, **110**, 8535.
23 R. Arrigo, M. Havecker, S. Wrabetz, R. Blume, M. Lerch, J. McGregor, E. P. J. Parrott, J. A. Zeitler, L. F. Gladden, A. Knop-Gericke, R. Schlogl and D. S. Su, *J. Am. Chem. Soc.*, 2010, **132**, 9616.
24 W. Gao, L. B. Alemany, L. J. Ci and P. M. Ajayan, *Nat. Chem.*, 2009, **1**, 403.
25 A. Bagri, C. Mattevi, M. Acik, Y. J. Chabal, M. Chhowalla and V. B. Shenoy, *Nat. Chem.*, 2010, **2**, 581.
26 G. Lota, K. Lota and E. Frackowiak, *Electrochem. Commun.*, 2007, **9**, 1828.
27 J. L. Figueiredo and M. F. R. Pereira, *Catal. Today*, 2010, **150**, 2.
28 H. P. Boehm, *Carbon*, 1994, **32**, 759.
29 J. L. Figueiredo, M. F. R. Pereira, M. M. A. Freitas and J. J. M. Orfao, *Carbon*, 1999, **37**, 1379.
30 X. R. W. X. R. Wang, X. L. Li, L. Zhang, Y. Yoon, P. K. Weber, H. L. Wang, J. Guo and H. J. Dai, *Science*, 2009, **324**, 768; K. P. Loh, Q. L. Bao, G. Eda and M. Chhowalla, *Nat. Chem.*, 2010, **2**, 1015.
31 B. Xu, S. F. Yue, Z. Y. Sui, X. T. Zhang, S. S. Hou, G. P. Cao and Y. S. Yang, *Energy Environ. Sci.*, 2011, **4**, 2826.
32 H. Zhu, X. L. Wang, F. Yang and X. R. Yang, *Adv. Mater.*, 2011, **23**, 2745; E. Raymundo-Piñero, M. Cadek, M. Wachtler and F. Béguin, *ChemSusChem*, 2011, **4**, 943.
33 L. Zhao, L. Z. Fan, M. Q. Zhou, H. Guan, S. Y. Qiao, M. Antonietti and M. M. Titirici, *Adv. Mater.*, 2010, **22**, 5202.
34 D. C. Wei, Y. Q. Liu, Y. Wang, H. L. Zhang, L. P. Huang and G. Yu, *Nano Lett.*, 2009, **9**, 1752; R. T. Lv, T. X. Cui, M. S. Jun, Q. A. Zhang, A. Y. Cao, D. S. Su, Z. J. Zhang, S. H. Yoon, J. Miyawaki, I. Mochida and F. Y. Kang, *Adv. Funct. Mater.*, 2011, **21**, 999.
35 D. W. Wang, F. Li, M. Liu, G. Q. Lu and H. M. Cheng, *Angew. Chem., Int. Ed.*, 2008, **47**, 373; F. Xu, R. J. Cai, Q. C. Zeng, C. Zou, D. C. Wu, F. Li, X. E. Lu, Y. R. Liang and R. W. Fu, *J. Mater. Chem.*, 2011, **21**, 1970.
36 C. W. Huang, C. H. Hsu, P. L. Kuo, C. T. Hsieh and H. S. Teng, *Carbon*, 2011, **49**, 895; G. H. Xu, C. Zheng, Q. Zhang, J. Q. Huang, M. Q. Zhao, J. Q. Nie, X. H. Wang and F. Wei, *Nano Res.*, 2011, **4**, 870.

